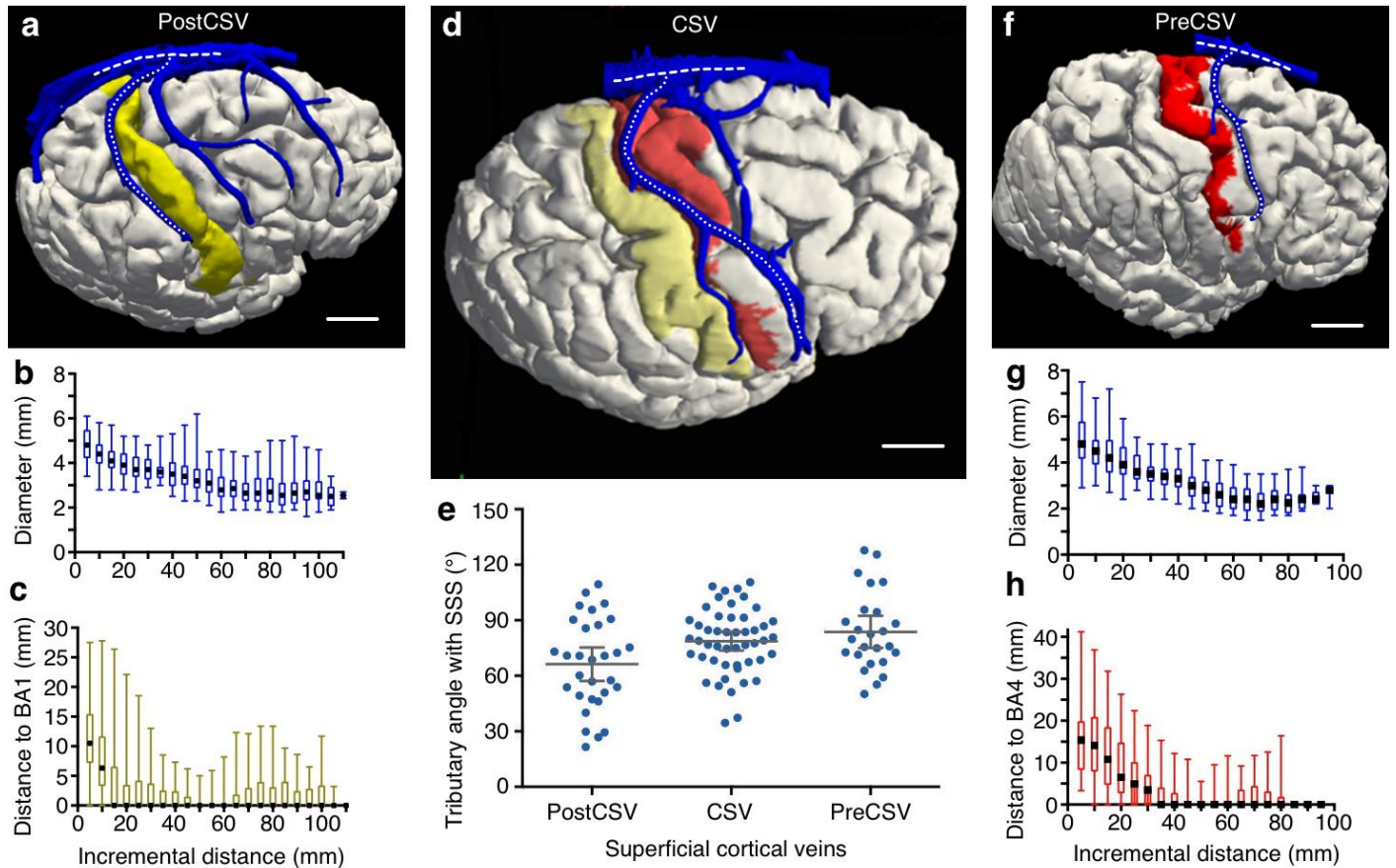**Supplementary Figure 1**

Human cerebral vein characterization

a, Superficial venous structures were identified and reconstructed using post-contrast brain MRI images (n=50). Scale bar, 3 cm. **b-c**, Vein diameters were manually measured using multi-planar image reconstructions at each 5 mm fiducial point along the course of the vein. Scale bar, 5 mm. **d**, Pial surfaces were reconstructed and segmented for primary motor (red, Brodmann Area, BA4) and sensory (yellow, BA1) areas. Scale bar, 3 cm. **e-f**, The shortest distance from each venous fiducial point to the pial surface of BA4 and BA1 was measured using multi-planar reconstructions. Scale bar, 3 mm. **g**, 3-dimensional reconstructed venous structures and motor and sensory surfaces were superimposed to position within sulci. Scale bar, 10 mm. **h**, Coronal view demonstrating superior sagittal sinus. Circle of best fit within triangular measurement was recorded as diameter at each fiducial point. Scale bar, 10 mm.

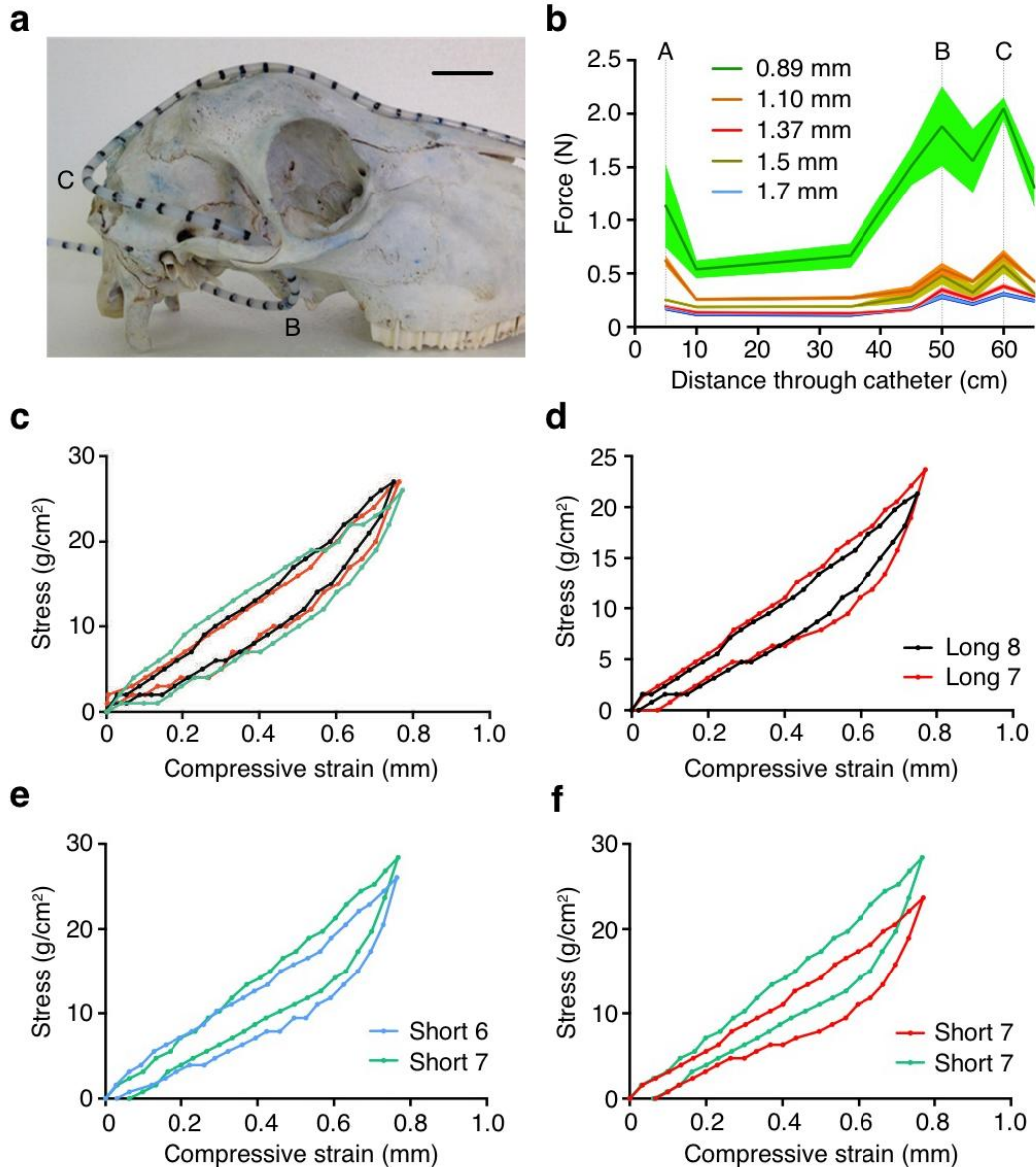**Supplementary Figure 2**

Human superficial cortical veins

a, Post-central sulcal vein (PostCSV, dotted line) reconstructed in relation to sensory cortex (yellow, Brodmann Area 1, BA1), with representative tributary feeding angle into superior sagittal sinus (SSS, dashed line). Scale bar, 2 cm. **b**, PostCSV lumen diameters at 5 mm increments, commencing proximally at SSS (median, IQR, range, n = 41). **c**, PostCSV distances to BA1 at 5 mm increments (median, IQR, range, n = 41). **d**, Central sulcal vein (CSV) route in relation to motor (red, BA4) and sensory (yellow, BA1) cortex. Scale bar, 2 cm. **e**, Angles of all veins entering SSS. PostCSV (mean 66.3° [95%CI 57.1 - 75.4], n = 30); CSV (mean 78.7° [95%CI 73.7 - 83.8], n = 49); PreCSV (mean 83.7° [95%CI 75.1 - 92.4], n = 25). **f-h,** Pre-central sulcal vein (PreCSV) diameters and distances in relation to motor cortex (red, BA4)(median, IQR, range). Scale bar, 2 cm.
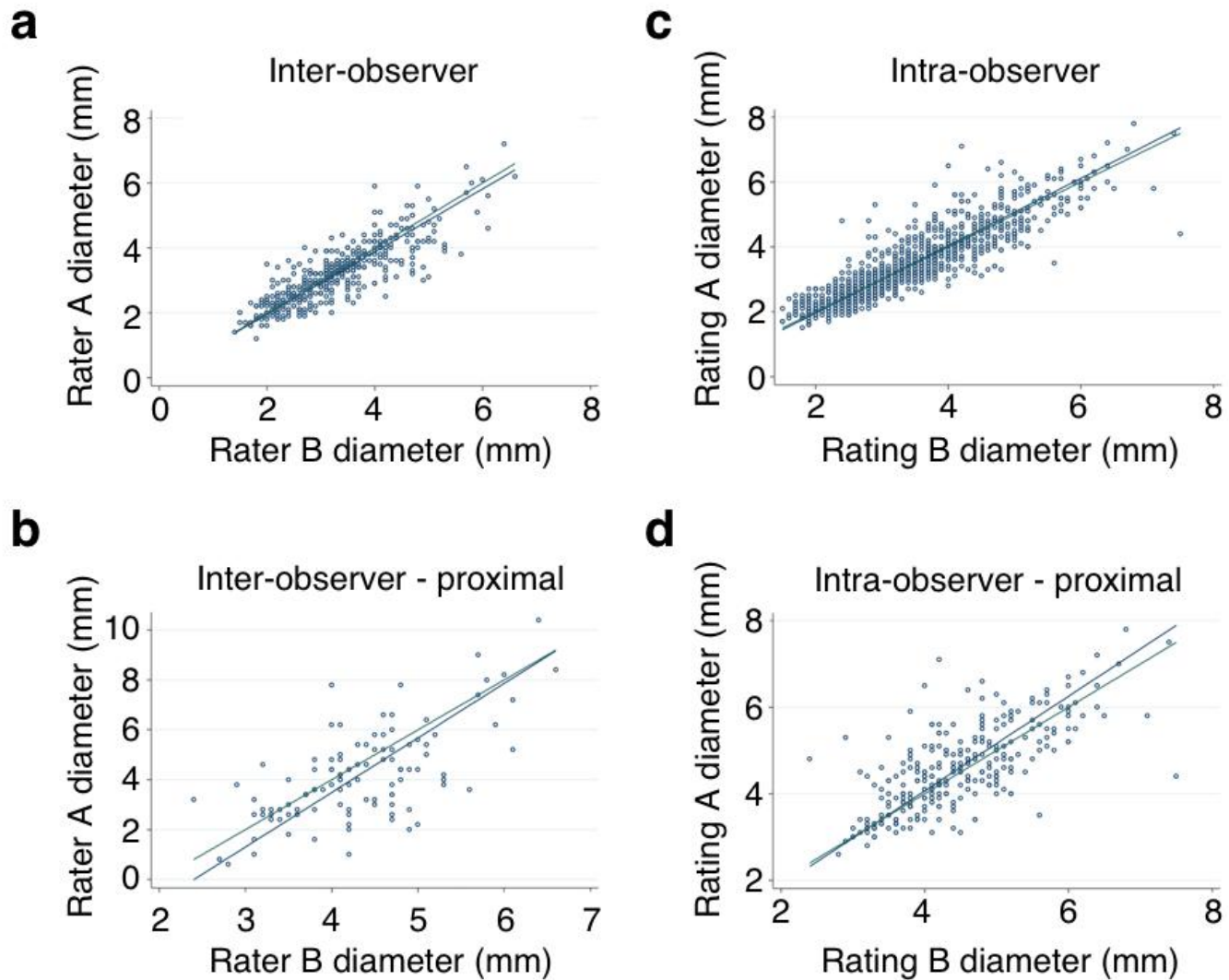
Supplementary Figure 3

Human vein diameter measurement reliability

a, Overall inter-observer reliability between two observers for superficial cortical vein diameter measurements were in almost perfect agreement (ICC = 0.84; Lin's CCC = 0.84 [95%CI 0.82 - 0.87]; reduced major axis slope = 0.97, intercept = 0.02). b, Proximal vein diameters demonstrated moderate-to-substantial agreement (ICC = 0.63; Lin's CCC = 0.63 [95%CI 0.53 - 0.75]; reduced major axis slope = 1.09, intercept = -0.63) with identifiable proportional bias. c, Overall intra-observer repeat diameter measurements were also in almost perfect agreement (ICC = 0.89; Lin's CCC = 0.89 [95%CI 0.88 - 0.9]; reduced major axis slope = 1.04, intercept = -0.11). d, Proximal vein region intra-observer diameters also demonstrated mildly lower values of agreement (ICC = 0.7; Lin's CCC = 0.7 [95%CI 0.64 - 0.76]; reduced major axis slope = 1.1, intercept = -0.3), indicative of substantial agreement.

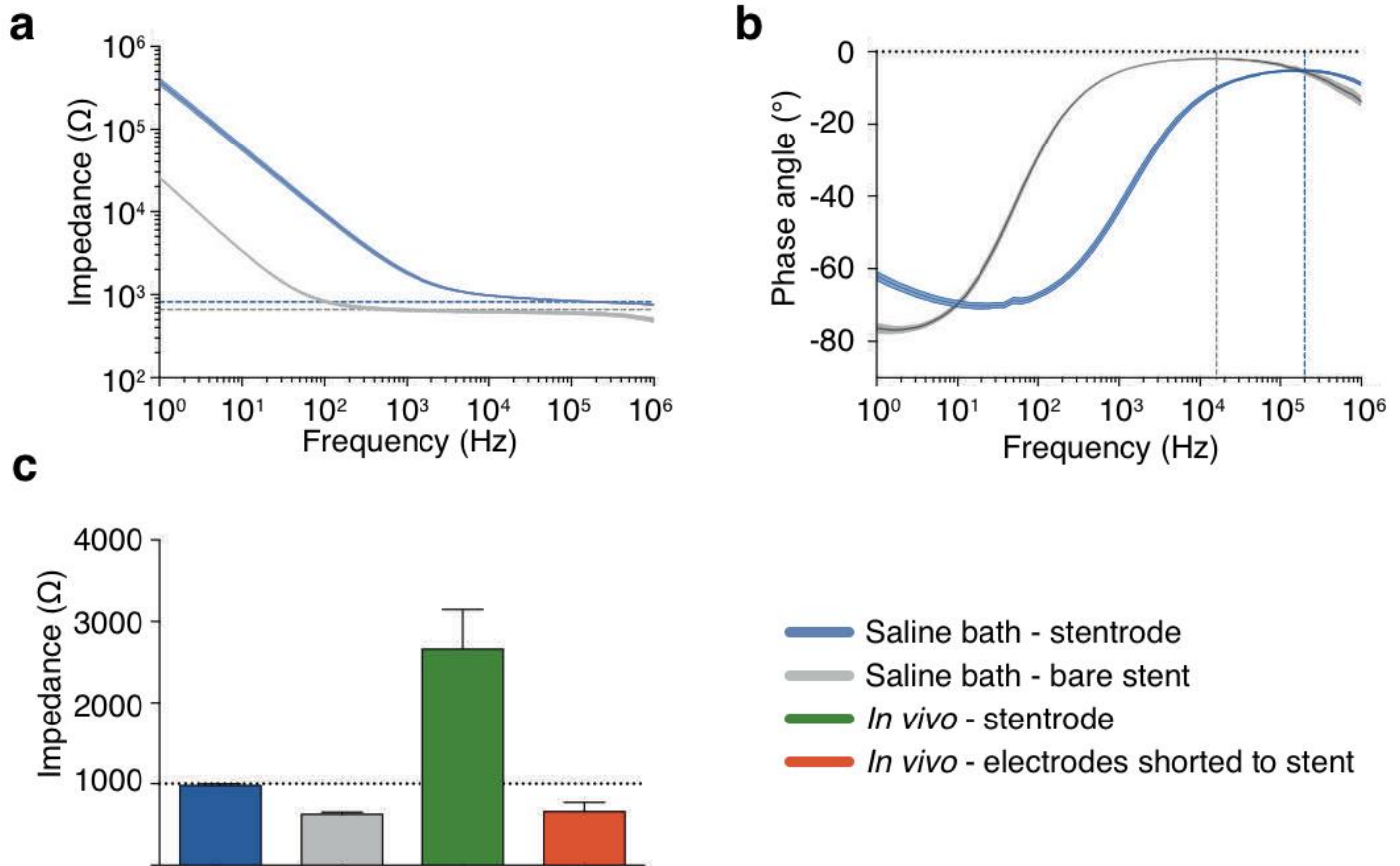## Supplementary Figure 4

Benchtop stentrode testing

a, Ovine vasculature mechanical model of major stress points along venous pathway indicating the jugular foramen (b) and the confluence of sinuses (c), scale bar, 1 cm. **b,** Internal catheter frictional force measured as stentrodes were deployed through catheters with varying internal diameters. Electrode detachment occurred only with attempts via 0.89 mm catheter (n = 3; all other catheter trials n = 9). **c,** Repeated measures (n = 3) compression test indicating superelasticity of stent is maintained with wire wrapping and attached electrodes. Average compression force comparison between **d,** long stentrodes with seven (n = 4) and eight (n = 4) electrodes, **e,** short stentrodes with six (n = 3) and seven (n = 4) electrodes and **f,** short and long stentrodes with seven electrodes each (n = 4).
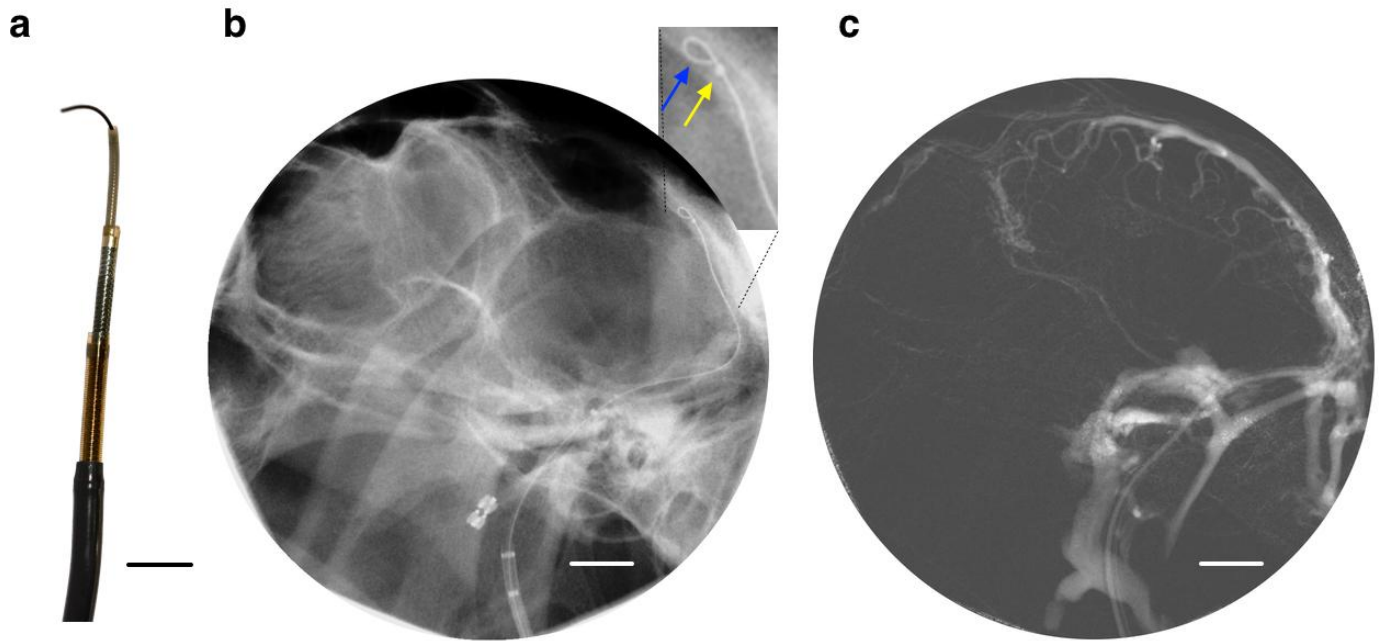
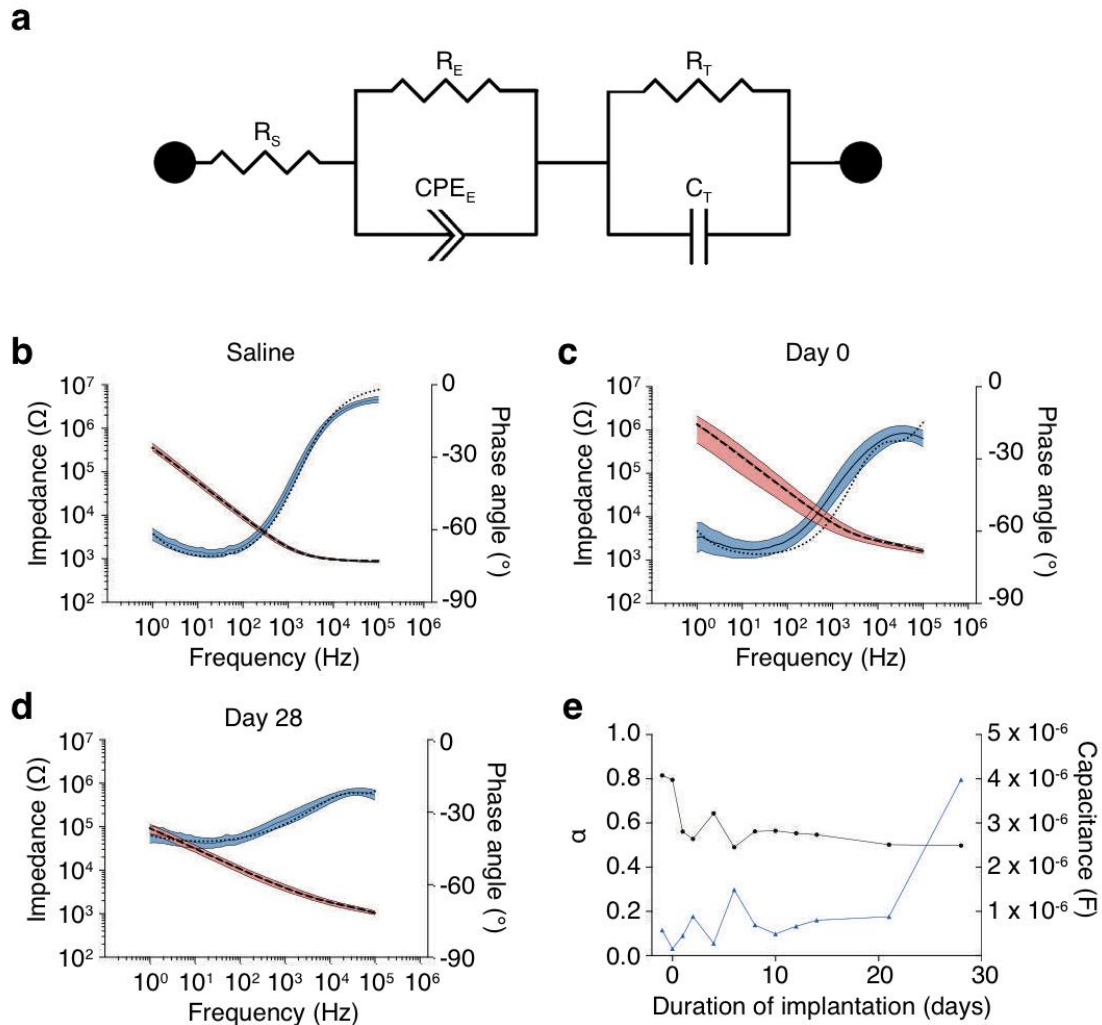**Supplementary Figure 5**

Coaxial catheter technique

a, Coaxial system including 6F sheath, 6F, 4F, 2F and microwire, all preloaded into one another. Commencing with microwire, entire system is telescoped over itself to negotiate the venous pathway toward the superior sagittal sinus (SSS). Scale bar, 5 mm. **b**, Plain x-ray demonstrating microwire (blue arrow) with a J shape to assist with negotiation of complex venous channels and bifurcations. 2F catheter (yellow arrow) is advanced over microwire to support entry into the SSS. Scale bar, 1 cm. **c**, Lateral projection digital subtraction angiography of SSS following access with 4F and prior to stentrode deployment. Scale bar, 1 cm.

Supplementary Figure 6

Identification of viable stent-mounted electrodes using electrochemical impedance spectroscopy

a, Impedance magnitude and **b,** phase angle of stentrode electrodes (blue) and bare metal stent (grey) immersed in saline [mean ± SD]. Dashed lines represent peak-resistance-frequency and access resistances for the stentrode electrodes (blue, 200 kHz and 816 ± 15 Ω [mean ± SD], n = 39 electrodes) and bare stent (grey, 16 kHz and 625 ± 27 Ω, n = 12 stents) immersed in saline. In saline, 10 kHz measurements are comparable with peak-resistance-frequency measured access resistance. **c,** Bar graph showing 10 kHz impedance of stentrode electrodes in saline (blue, 979 ± 20 Ω [mean ± SD], n = 39 electrodes), bare metal stents in saline (grey, 625 ± 27 Ω, n = 12 stents), stentrode *in vivo* immediately following implantation (green, 2662 ± 486 Ω, n = 28 electrodes) and stentrode *in vivo* with electrodes shorted to the stent (red, 659 ± 113 Ω, n = 7 electrodes). Dashed black line at 1 kΩ indicates *in vivo* electrode exclusion criteria for viability.

Supplementary Figure 7

Equivalent circuit model of electrode-tissue interface in comparison to saline bath and *in vivo* measurements

a, Simple equivalent circuit model showing solution resistance (R_S), electrode-tissue interface charge transfer resistance (R_E) and double-layer capacitance constant phase element (CPE_E), and the tissue resistance (R_T) and capacitance (C_T). **b,** Comparison between equivalent circuit model impedance (dashed black line) and phase (dotted black line) and electrochemical impedance spectroscopy measurements [mean ± 95%CI] of average impedance (red) and phase angle (blue) of stentrodes immersed in saline (n = 39 electrodes) and *in vivo* at **c,** Day 0 (n = 28 electrodes) and **d,** Day 28 (n=33 electrodes). **e,** Change in *α* (black trace) and capacitive magnitude (*F*, blue trace) of the constant phase element as a function of implant duration, suggestive of incorporation and adherence of proteins to the electrode-tissue interface.
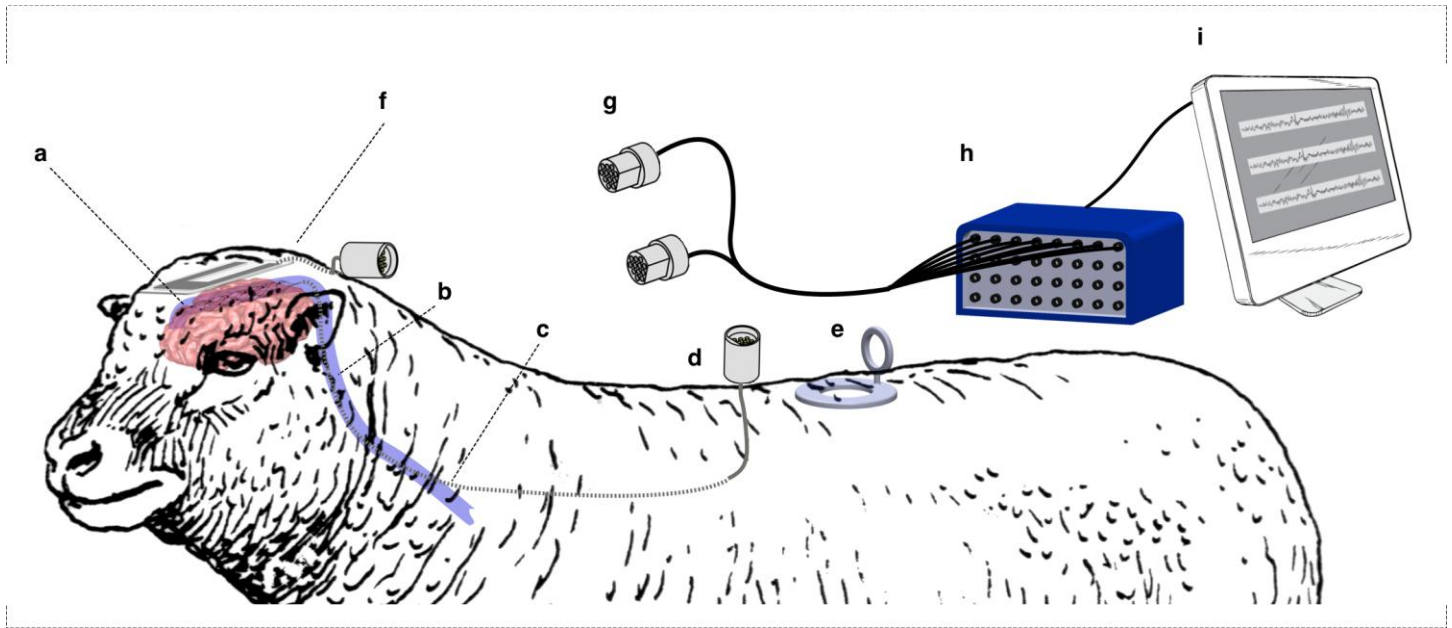
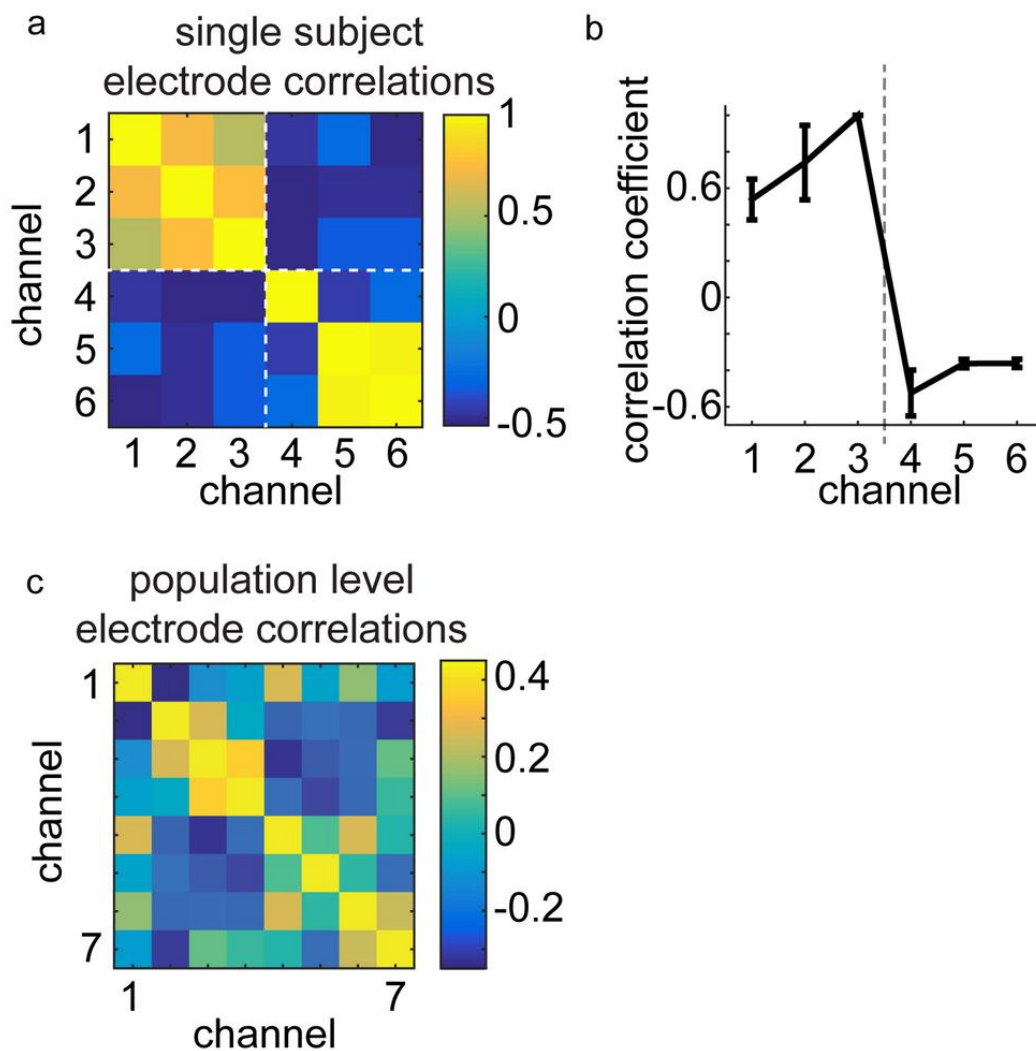## Supplementary Figure 8

Schematic of experimental set up

a, Endovascular stent-electrode array (stentrode) is shown implanted within the superior sagittal sinus within the brain. **b,** The electrode lead wire is shown to exit the brain within the internal jugular vein. **c,** The lead wire protrudes through the wall of the common jugular vein in the neck, and tunnels subcutaneously to **(d)** a custom-made hermetic connector secured to a muscle, and exiting the skin in a percutaneous micro circular plug (Omnetics, Minneapolis MN, USA). **e,f,** Two ground electrodes implanted subcutaneously: a large, stainless steel ground electrode implanted in the back of the sheep **(e)**, and a platinum c-shaped ground electrode under the scalp in close proximity to the stentrode **(f)**. Electrode lead wires and ground electrodes are connected to omnetics connectors **(g)** that are connected to a data acquisition system (TMSi Porti, Twente Medical Systems International, Oldenzaal, Netherlands) **(h)** and computer **(i)** to record neural information.
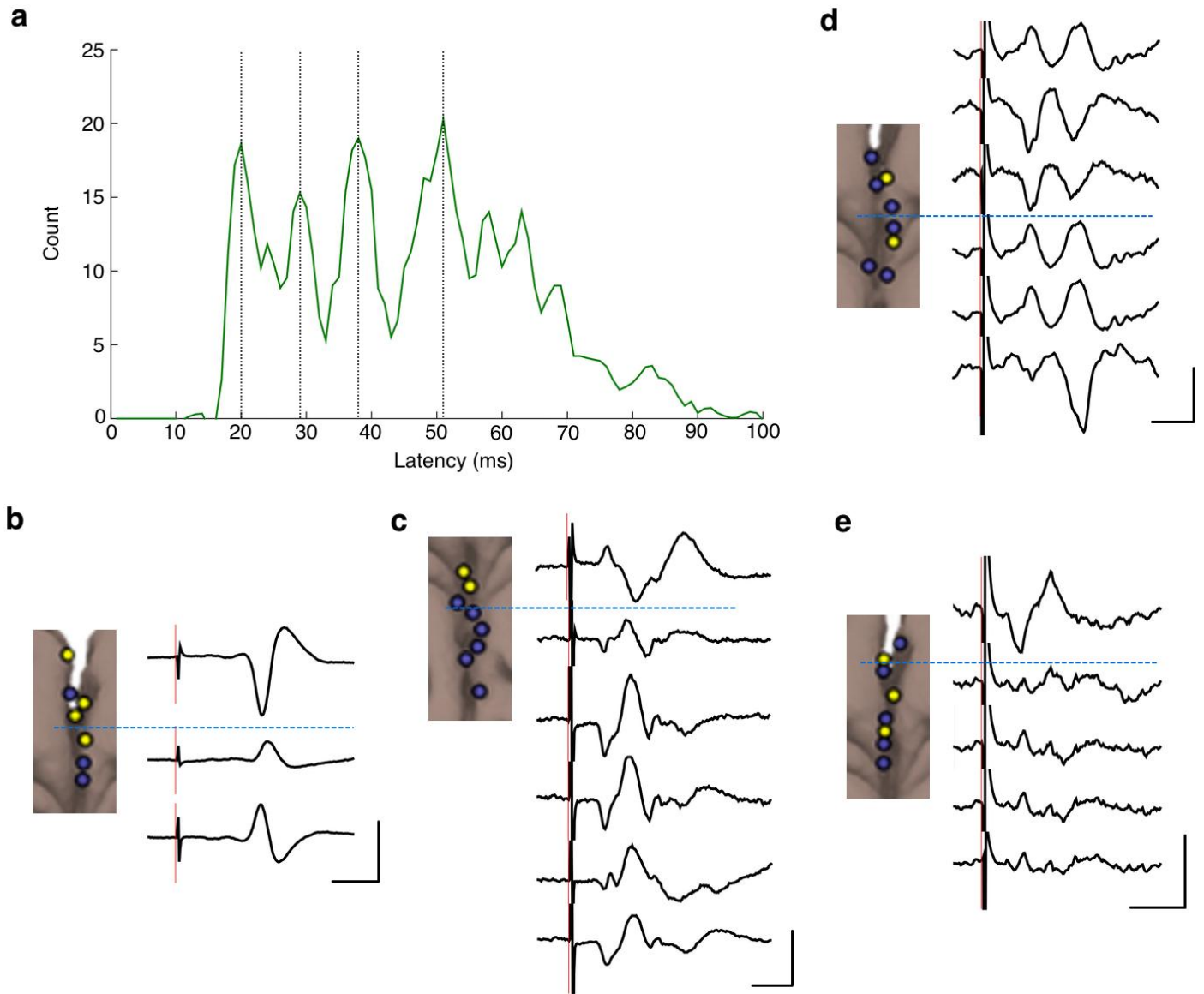
Supplementary Figure 9

Somatosensory evoked potential latencies

**a,** Histogram of all rectified peak latencies (n = 703 peaks, n = 5 animals, n= 57 [40-70] trials/session [median, interquartile range]) demonstrating occurrence of physiological peaks at 20 ms, 28 ms, 38 ms and 51 ms. **b-d**, Representative SSEP morphologies from individual subjects by individual electrode (**b,** S4; **c,** S2; **d,** S3; **e,** S1). Insert image displays the distribution of electrodes per subject within the superior sagittal sinus (blue circles, functional and represented electrodes). Blue dashed line represents phase reversal and dipole between peaks. Scale bar, 40μV, 20 ms.

Supplementary Figure 10

Stentrode electrode correlation coefficients

a, Image plot of the correlation coefficients between electrodes for an example subject. Electrodes (n = 6) on the rostral end of the electrode were positively correlated with each other (yellow, > 0.5), with signals on the caudal end of the array exhibiting a phase shift reflected in the negative correlation coefficients (blue, < 0). **b,** Correlation coefficients of electrodes (n = 6) from an example subject (mean, SEM) showing a positive to negative change in correlation coefficient indicative of electrode location and phase shift of the acquired signal. **c,** Population average [mean] image plot of the correlation coefficients (n = 31 electrodes in 5 animals) showing electrodes with high correlation (yellow, >0.2) and low correlation (blue, < 0). The maximum of the color scale has been reduced to 0.45 to allow for easier comparisons, however coefficients for all electrodes against themselves (diagonal values) are 1.
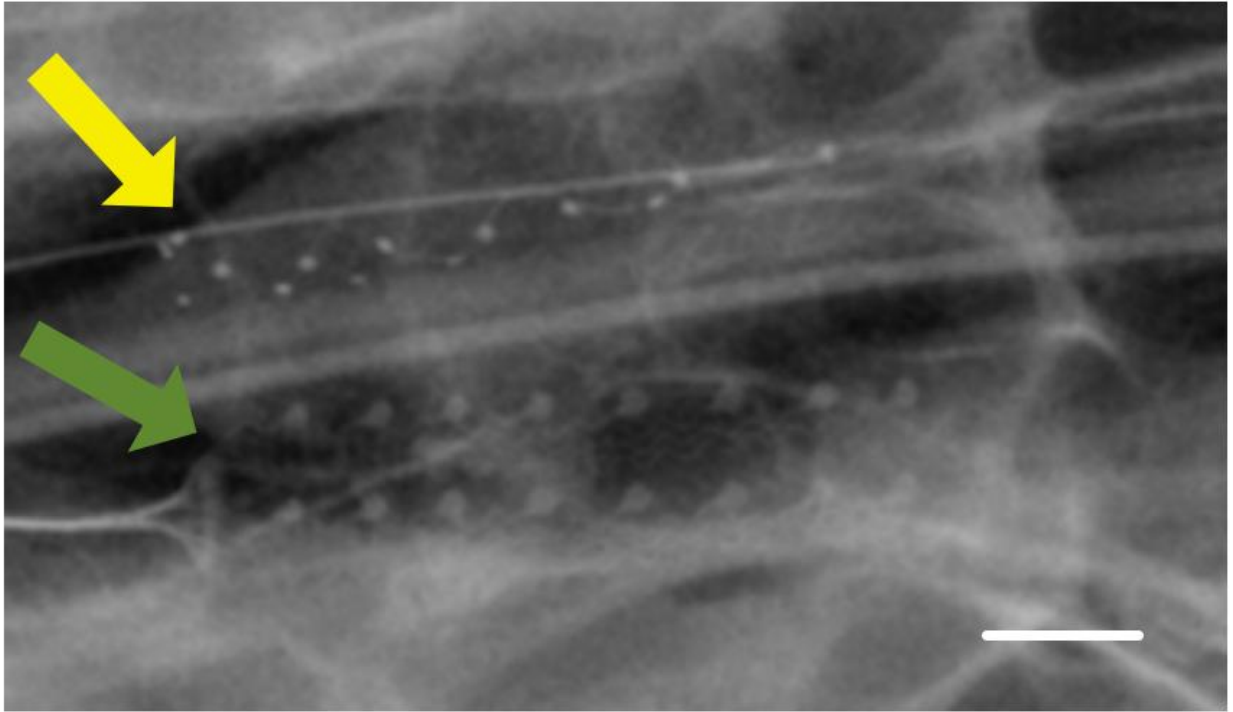
Supplementary Figure 11

Validation ECoG recordings from stentrode and epidural array

Representative example demonstrating x-ray of co-implanted stentrode (yellow arrow) and epidural array (green arrow) for validation recording acute experiments. Scale bar, 5 mm.
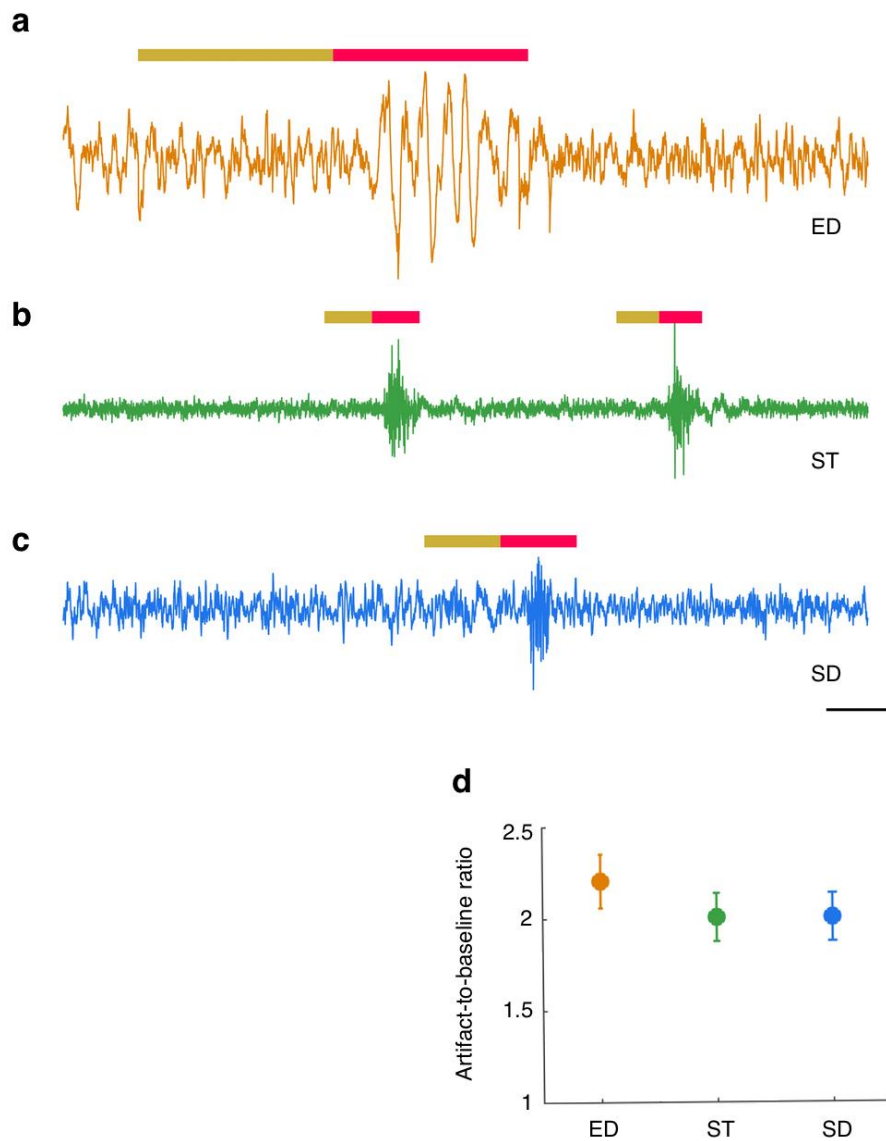
Supplementary Figure 12

Chewing artifact comparison between recording arrays

Individual raw ECoG recordings from **a,** epidural (ED, orange), **b,** endovascular stentrode (ST, green) and **c,** subdural (SD, blue) electrode arrays. Red boxes indicate the identified chewing artifacts and the brown boxes indicate the baseline period. Scale bar, 50 µV, 500ms. **d,** Artifact-to-baseline ratio for the epidural arrays (2.2 ± 0.1, n = 29 electrodes in 3 sheep), stentrode arrays (2 ± 0.1 [mean $\pm$ SE] n = 49 electrodes in 11 sheep) and subdural arrays (1.8 ± 0.1, n = 30 electrodes in 6 sheep). A Tukey-corrected one-way ANOVA showed that there was no statistically significant difference between the subdural, epidural, or stentrode arrays (p=0.109).